AGU PUBLICATIONS

Geophysical Research Letters

RESEARCH LETTER
10.1002/2014GL059453

Key Points:
- Satellite-retrieved convective cloud base drop concentration was validated
- Cloud base CCN were retrieved when adding cloud-radar-measured updraft
- Satellite with radar-retrieved CCN at cloud base validated at the DOE/SGP site

Correspondence to:
D. Rosenfeld,
daniel.rosenfeld@huji.ac.il

Citation:
Rosenfeld, D., B. Fishman, Y. Zheng, T. Goren, and D. Giguzin (2014), Combined satellite and radar retrievals of drop concentration and CCN at convective cloud base, *Geophys. Res. Lett.*, *41*, 3259–3265, doi:10.1002/2014GL059453.

Received 28 JAN 2014
Accepted 28 MAR 2014
Accepted article online 1 APR 2014
Published online 7 MAY 2014

Combined satellite and radar retrievals of drop concentration and CCN at convective cloud base

Daniel Rosenfeld[1], Baruch Fischman[1], Youtong Zheng[1,2], Tom Goren[1], and David Giguzin[1]

[1]Institute of Earth Sciences, Hebrew University of Jerusalem, Jerusalem, Israel, [2]Department of Atmospheric and Oceanic Science and Earth System Science Interdisciplinary Center, University of Maryland, College Park, Maryland, USA

Abstract The number of activated cloud condensation nuclei (CCN) into cloud drops at the base of convective clouds (N_a) is retrieved based on the high-resolution (375 m) satellite retrievals of vertical profiles of convective cloud drop effective radius (r_e). The maximum cloud base supersaturation (S) is calculated when N_a is combined with radar-measured updraft and yields CCN(S), which was validated well against ground-based CCN measurements during the conditions of well-mixed boundary layer over the U.S. Department of Energy's Atmospheric System Research Southern Great Plains site. Satellite retrieving N_a is a new capability, which is one essential component of simultaneous measurements of cloud microstructure and CCN from space by using clouds as natural CCN chambers. This has to be complemented by a methodology for satellite estimates of cloud base updraft, which is yet to be developed and demonstrated. In the mean time, the retrieved N_a can be used for the assimilation of the combined CCN and updraft effects on clouds in models.

1. The Motivation for Satellite Retrievals of Cloud Base Drop Concentrations

Disentangling the effects of aerosols and meteorology on cloud radiative effects is a major challenge that impedes us from quantifying the aerosol cloud-mediated climate forcing and therefore constitutes the largest source of uncertainty in anthropogenic climate forcing [*Rosenfeld et al.*, 2014]. This disentanglement requires simultaneous measurements of cloud condensation nuclei (CCN) and cloud microphysical and dynamical properties from space, as envisioned by the CHASER (Clouds, Hazards, and Aerosols Survey for Earth Researchers) satellite mission [*Rosenfeld et al.*, 2012; *Rennó et al.*, 2013]. The main idea of CHASER is using the base of convective clouds as CCN chambers. Measuring both the number concentrations of activated CCN into cloud drops at cloud base (N_a) and the updraft speed there (W_b) yields the vapor supersaturation (S) that the CCN particles are exposed to. Therefore, in fact, N_a is the number concentration of CCN activated at S, i.e., CCN(S). This study represents a step toward the goal of satellite retrievals of CCN(S).

Until now, satellite-retrieved cloud drop number concentrations (N_d) were based on vertically integrated cloud properties, such as liquid water path and optical depth [e.g., *Szczodrak et al.*, 2001; *Bennartz*, 2007]. Therefore, the retrieved N_d had to assume spatial homogeneity of the clouds, which is valid for layer much more than convective clouds. Furthermore, the mixing of the cloud with ambient air as it grows above its base dilutes N_d to much smaller values than N_a.

Retrieving N_a has become possible with the recent launch of the Suomi NPP (National Polar-Orbiting Partnership) satellite. The imager of the VIIRS (Visible Infrared Imaging Radiometer Suite) makes it possible by its breakthrough resolution of wave bands that allows retrieving cloud microstructure with the methodology that was developed by *Rosenfeld et al.* [2013]. The satellite resolution is 375 m at nadir, with little degradation across the swath. Although the standard VIIRS cloud products are available only at the moderate resolution of 750 m, *Rosenfeld et al.* [2013] developed a methodology to retrieve cloud properties at the VIIRS imager resolution of 375 m, which is used in this study. This resolution means a pixel area of only one seventh of a similar pixel of the Moderate Resolution Imaging Spectroradiometer (MODIS). The pixel area's ratio of VIIRS imager/MODIS reduces to nearly 0.05 away from nadir at the edge of the swath. This high resolution allows retrieving the cloud drop effective radius (r_e) of small convective elements that would fill only very partially MODIS pixels and provide realistically looking cloud microstructure starting from very near the cloud base [*Rosenfeld et al.*, 2013]. The determination of cloud base is very accurate. The cloud base temperatures were retrieved by the VIIRS imager at accuracy of ±1.1°C [*Zhu et al.*, 2014]. This was used for the calculation of cloud base temperature, because the radisonde time was 1.5 to 2 h earlier.

©2014. American Geophysical Union. All Rights Reserved.

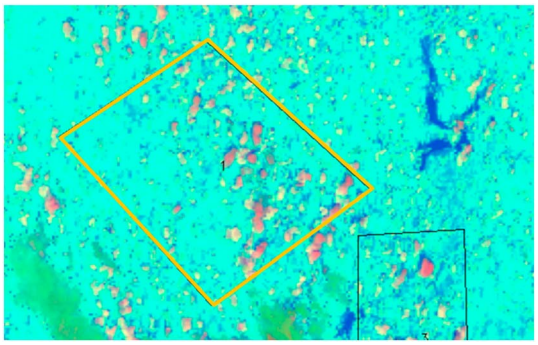


Figure 1. NPP/VIIRS high-resolution (375 m) image of the analyzed area (yellow rectangle) centered at the SGP site, at 16 July 2013, 19:37 UT. The rectangle size is about 35 × 45 km. The color scale is microphysical red-green-blue, where clouds with larger r_e appear redder. The red modulates the visible reflectance, green the 3.7 μm solar reflectance, and blue modulates the 10.8 μm brightness temperature, as done by *Rosenfeld et al.* [2013].

The VIIRS imager-based high-resolution-retrieved cloud properties allow also retrieving the number concentrations of CCN at cloud base (N_a) with the methodology that is described in section 2. The cloud base height, temperature, and updraft speeds are measured by ground-based radar, lidar, ceilometer, and satellite that were validated by radiosondes [*Zhu et al.*, 2014] at the U.S. Department of Energy's (DOE) Atmospheric System Research Southern Great Plains (SGP) site, as described in section 3. The closure calculations with the ground-based-measured CCN(S) are described in section 4. Finally, conclusions are provided in section 5.

2. Retrieving the Number of Activated CCN at Cloud Base

Aircraft observations showed that the vertical evolution of convective cloud r_e often does not deviate much from the value that it would have in an adiabatic cloud parcel in which all cloud drops nucleate at its base, and continued growth occurs exclusively by condensation [e.g., *Paluch*, 1986; *Pawlowska et al.*, 2000; *Burnet and Brenguier*, 2007]. This was explained by cloud mixing mode that is close to extreme inhomogeneous. Some other studies showed a smaller-drop growth rate with height that indicates a larger component of homogeneous mixing [e.g., *Paluch and Baumgardner*, 1989], although part of this component may be explained by instrumental artifacts [*Burnet and Brenguier*, 2007]. An extensive survey of aircraft measurements in the Amazon, California, India, and Israel showed the dominance of the near-extreme inhomogeneous mixing mode [*Freud et al.*, 2011]. N_a was calculated by *Freud et al.* [2011] as follows:

$$N_a = \alpha^3 \mathrm{LWC}_a / {r_{ea}}^3 \tag{1}$$

$$\alpha = 62.03 \ \ r_e / r_v \tag{2}$$

where LWC_a is the cloud adiabatic liquid water content, r_{ea} is the cloud drop adiabatic r_e, and r_v is the cloud drop mean volume radius, as calculated by distributing equally LWC between the observed cloud base maximum N_d. There is a tight relation between r_e and r_v, where $r_e = 1.08\, r_v$ over all the nonprecipitating clouds that were analyzed by *Freud et al.* [2011].

Freud et al. [2011] compared the aircraft-observed N_d near cloud base to the calculated value of N_a based on the assumption of extreme inhomogeneous mixing using equation (1) and found that N_d and N_a were highly correlated ($R = 0.96$) with an average overestimation bias of N_a with a factor of 1.3 with respect to the cloud base N_d. This bias is likely due to deviations from the mode of extreme inhomogeneous mixing.

Growth of cloud drops by coalescence violates the assumptions at the basis of calculating N_a. Using the same aircraft data, *Freud and Rosenfeld* [2012] showed that the coalescence rate is proportional to ${r_e}^{4.8}$, which means that practically, coalescence has insignificant impact on the growth rate of r_e and initiation of rain up to a certain threshold value of r_e. This value was found to be around 14 μm [*Freud and Rosenfeld*, 2012]. Therefore, the cloud portions below the height, where r_e exceeds 14 μm, can be used for retrieving N_a.

Rosenfeld et al. [2012] proposed to use the same methodology of calculating N_a based on high-resolution satellite-retrieved r_e. This was actually done in this study based on the retrieved r_e from the VIIRS imager, using the retrieval methodology of *Rosenfeld et al.* [2013]. In addition to the retrieved r_e, which is a proxy for r_{ea}, the calculation of N_a, as shown in equation (1), requires the knowledge of LWC_a, which requires in turn the knowledge of cloud base temperature and pressure. LWC_a as a function of cloud temperature is calculated by a parcel model. The cloud base height was measured by the ceilometer at the SGP site during the satellite overpass time (around 13:30 solar time or 19:30 UT), and the temperature at that height was obtained from the sounding that is available from 2 h earlier, at 17:30 UT.

©2014. American Geophysical Union. All Rights Reserved.

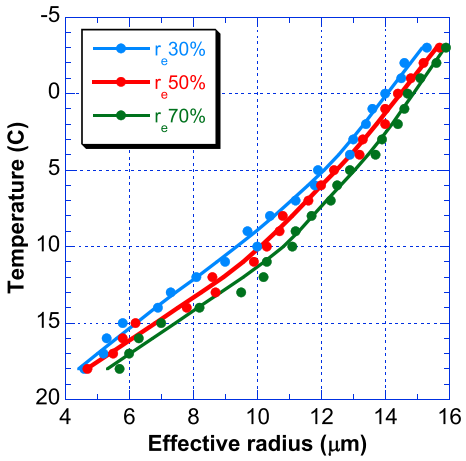


Figure 2. The T-r_e relations of the clouds over the SGP site within the rectangle shown in Figure 1. The different lines are denoted as the percentiles of r_e for the same cloud top temperature, T.

An example for a case study is given here for 16 July 2013 over the SGP site. The cloud top temperature (T)-r_e relations are obtained for the rectangle shown in Figure 1, using the same color code and methodology as done by *Rosenfeld et al.* [2013]. This particular rectangle has 1502 measured pairs of T and r_e. The r_e values for each 1°C interval of T are sorted. The 30th, 50th, and 70th percentiles of r_e are plotted as a function of T, as shown in Figure 2. The adiabatic water profile, $LWC_a(T)$, was calculated based on the cloud base temperature and pressure, as obtained from the ceilometer and sounding. Then, N_a is calculated based on equation (3).

$$N_a = LWC_a / Mr_{va} \tag{3}$$

where Mr_{va} is the mass of a cloud drop with an adiabatic r_v, which is calculated as

$$Mr_v = (4/3)\rho\pi(r_e/1.08)^3 \tag{4}$$

where ρ is the water density.

The calculation of N_a is illustrated in Figure 3 as the slope of the relation between the cloud drop mass and the cloud liquid water content. Mr_v, the drop mass as calculated for r_v of each r_e percentiles for a given T using equation (4), is plotted against LWC_a for the same T, as shown in Figure 3. The value of r_v is taken as r_e/1.08 [*Freud et al.*, 2011]. In an ideal adiabatic rising cloud parcel, LWC_a should increase linearly with cloud drop mass. Therefore, a linear best fit is calculated between LWC_a and Mr_v, as shown in Figure 3. According to equation (3), the slope of the best fit line corresponds to the adiabatic drop concentrations, which is in fact N_a. The calculated line of best fit is forced to zero at $LWC_a = 0$. The calculated r_e for cloudy pixels that are close to cloud base may be distorted due to surface contamination. Therefore, skipping the lowest points improves the accuracy of the calculation. In principle, it is sufficient to connect one point at cloud top to the cloud base for obtaining the line and the respective N_a. The value of the calculated N_a is divided by 1.3 to account for the mean deviation from the assumption of extreme inhomogeneous mixing [*Freud et al.*, 2011].

According to equation (3) and as illustrated in Figure 3, N_a values that are calculated based on higher percentiles of r_e or r_v are larger. The units of LWC_a and N_a are expressed in mixing ratios, so that the changes in air density with height would not be a factor in the calculated values.

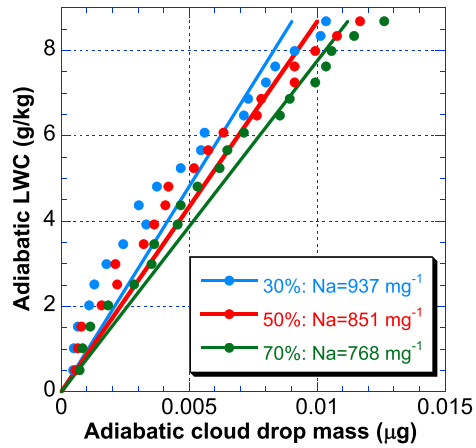


Figure 3. The calculation of number of activated cloud drops, N_a, based on the T-r_e relations shown in Figure 2. N_a is the slope of the relation between adiabatic cloud water and the mass of an adiabatic cloud drop, as shown in equation (3). The calculated N_a values for different percentiles of r_e for a given T are shown in the legend.

3. The Measurements of Cloud Base Updraft

The cloud base updraft speeds were calculated based on vertically pointing Ka-band Doppler cloud radar at the SGP. Cases with rain were excluded, because the falling raindrops dominate the Doppler radar signal. The formulation of the effective updraft speed at a given volume of air that has multiple radar pixels is given as

$$W = \left. \frac{\sum N_i W_i^2}{\sum N_i W_i} \right|_{W_i > 0} \tag{5}$$

where N_i stands for the frequency of occurrence of the vertical velocity W_i. Stronger updrafts produce, respectively, larger cloud volume per unit area of cloud base. Equation (5) weighs the cloud volume with respect to the updraft speed that created it. Therefore, W_b (cloud base updraft) that is calculated in equation (5) is the cloud physics relevant updraft, if it is to be expressed by a single number.

©2014. American Geophysical Union. All Rights Reserved.

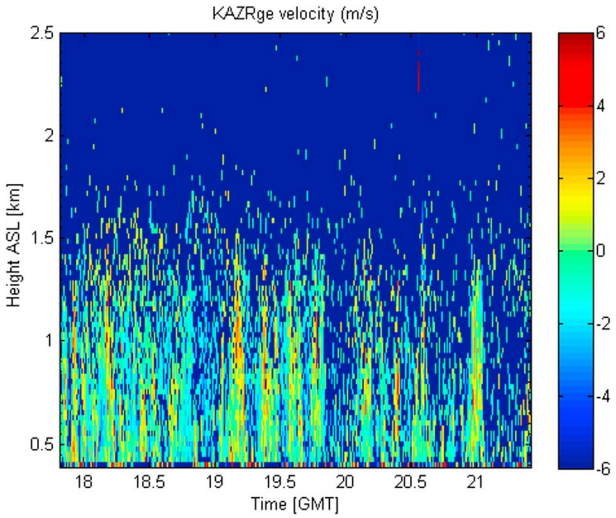


Figure 4. The Doppler velocities measured by a vertically pointing cloud radar at the SGP site on 16 July 2013, for the clouds shown in Figure 1. The scale is vertical velocity in ms^{-1}. The satellite overpass occurred at 19.61 (decimal hour) UT. The clouds are not detected because their drop sizes are below the detection limit of the radar. The updraft speed near cloud base (±200 m) at the overpass time ±1 h was 1.56 ms^{-1}.

An example of the radar-measured W structure of the boundary layer is given in Figure 4. W_b is calculated using equation (5) based on the Doppler data measured within a time window of ±1 h from the satellite overpass time and a height window of ±200 m of the cloud base height. Figure 5 shows the micropulse lidar backscatter for the same case. The cloud base is evident clearly at a height of about 1.5 km above sea level in the lidar image, but is not discernible in the radar image (Figures 4 and 5, respectively). The reason is the very small cloud drops, as evident in Figure 2, which have reflectivity much below the radar minimum detectable signal.

4. Validation and Closure of Satellite-Retrieved N_a With CCN(S)

Next step is validating the calculated CCN(S) against the surface-based instruments at the SGP site. At this stage, we have W_b from radar measurements, along with satellite-retrieved N_a. Lidar Doppler measurements were not used here because they were not available for some of the cases. *Pinsky et al.* [2012] introduced an expression (equation (6)) that shows how to use W_b and N_a for calculating the maximum supersaturation at cloud base:

$$S = CW_b^{3/4}N_a^{-1/2} \tag{6}$$

where the coefficient C depends on the cloud base temperature and pressure.

The application of equation (6) for a given N_a and W_b results in a respective value of CCN(S). Since we have four percentiles of $r_e(T)$, four respective CCN(S) are calculated, for showing the sensitivity of the percentiles. We take the 50th percentile (median) as the most representative one and use this from here onward.

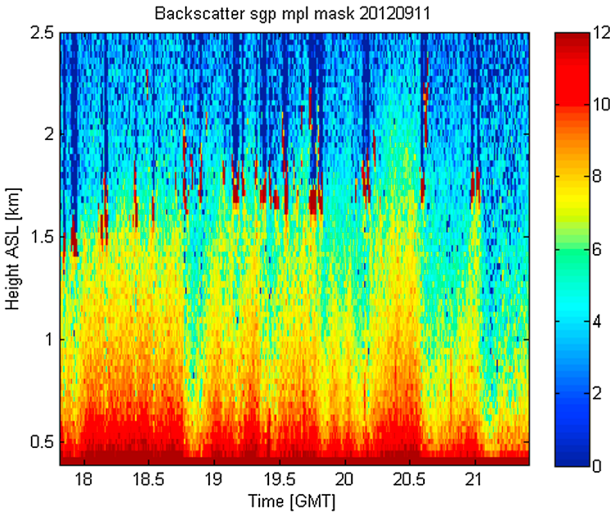


Figure 5. Vertically pointing lidar for the same scene shown in Figure 4. The colors show the signal-to-noise ratio. Clouds are seen between 1.4 and 2 km above sea level.

The comparisons of surface with cloud base measurements may be valid only if there is a well-mixed boundary layer. This was verified for the selected case studies by a vertical continuity of the radar and lidar features between the surface and cloud base and by having a radiosonde uninterrupted dry adiabatic lapse rate between the ground and cloud base height.

Two instruments were available for measuring CCN at the SGP site: a CCN counter based on diffusion-generated supersaturation in a column and a tandem DMA (differential mobility analyzer). The latter instrument provided much more detailed CCN measurements extending to lower supersaturations. The cloud base CCN(S) in units of mg^{-1} had to be converted to cm^{-3} at the

©2014. American Geophysical Union. All Rights Reserved.

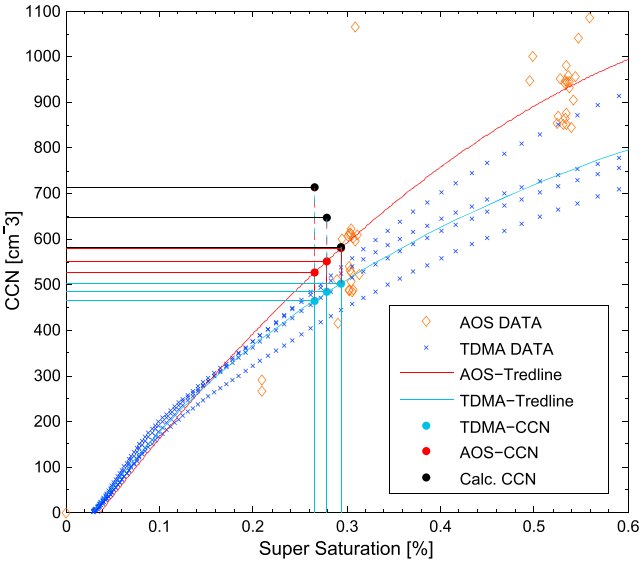


Figure 6. The matching between satellite-retrieved and surface-measured CCN for the case shown in the previous figures. The cloud base supersaturations (S) of the 30th, 50th, and 70th r_e percentiles for a given T are shown by the vertical blue lines, where a higher percentile pertains to a higher S. The satellite-retrieved N_d values are shown as the black horizontal lines. Their intersections with the vertical S lines are shown by black circles, which denote the satellite-calculated CCN(S) for the different percentiles. The blue intersections show the CCN(S) as measured by the tandem DMA during four measuring cycles. The solid thin blue curve is the best fit line of the TDMA measurements. The blue circles show the ordinate of the TDMA-measured CCN values for the cloud base S. The red circles show the same for the measurements of the CCN diffusion chamber (AOS), to which the satellite-calculated CCN concentrations should be compared. For example, for the 50th percentile: $S = 0.32\%$, satellite-calculated CCN = 647 cm^{-3}, AOS-measured CCN = 552 cm^{-3}, and TDMA-measured CCN = 483 cm^{-3}.

surface air density for compatibility with the units of the ground-based measurements. The retrieved and instrument-measured CCN for the same S as calculated in equation (6) were compared, as shown in Figure 6. For example, the values for the 50th T-r_e percentiles for the case shown in Figures 1–6 were $S = 0.32\%$, satellite-calculated CCN = 680 cm^{-3}, aerosol observing system (AOS) diffusion chamber-measured CCN = 635 cm^{-3}, and tandem DMA (TDMA)-measured CCN = 540 cm^{-3}. The median values for the case study and for the other analyzed cases are given in Table 1 and plotted in Figure 7.

All available suitable cases from the launch of the NPP/VIIRS on 28 October 2011 were analyzed. Only eight cases met all the selection criteria, which were the following:

1. Satellite zenith angle has to be between 0 and 45° to the east of the ground track, which is the sunny side of the clouds. This is required due to the large three-dimensional effects when staring at convective clouds with the Sun not in the back. Specifically, when the Sun is not in the back, the topography of the cloud tops creates many shadowed areas that distort the retrieved values. These satellite views for a specific location occur once or twice every 6 days.
2. The occurrence of convective clouds with vertical development that span at least 6°C of cloud temperature.
3. Well-mixed boundary layer, with vertical continuity of the air between the surface and cloud base. The vertical continuity was tested by requiring a dry adiabatic lapse rate between the surface and cloud base height and having visibly vertical continuity of the thermals between the ground and cloud base, as seen in the radar and lidar images. The condition of vertical continuity was often

Table 1. Summary of the Case Studies[a]

Date: dd/mm/yyyy	S (%)	Updraft (ms^{-1})	CCN TDMA	SGP-CCN AOS (cm^{-3})	Satellite-retrieved-CCN (cm^{-3})
13/7/12	0.36	2.99	1416	1666	1419
18/7/12	0.44	2.91	840	947	734
19/7/12	0.37	2.27	689	724	908
28/7/12	0.43	2.80	NA (not available)	1106	814
19/5/13	0.14	0.83	NA	1071	989
16/7/13	0.28	1.56	483	552	647
22/7/13	0.33	1.61	NA	1160	505
26/7/13	0.28	1.08	NA	439	361

[a]The SGP CCN is based on the TDMA and on the diffusion chamber (AOS). The S and satellite CCN are for the median r_e.

©2014. American Geophysical Union. All Rights Reserved.

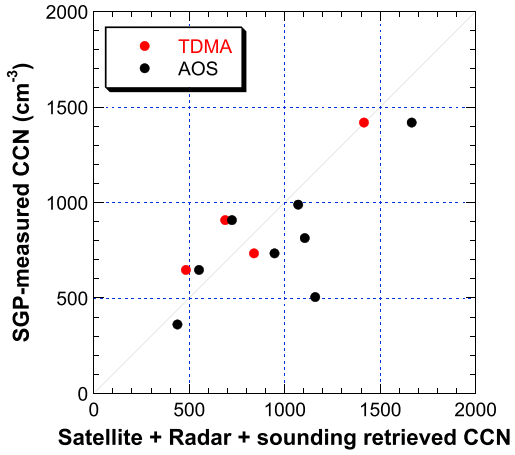


Figure 7. Validation of the satellite with radar-retrieved CCN against the SGP-measurements, for all the available cases.

not fulfilled when the dry line was in the area and elevated convection occurred above a lower level inversion.

4. Nonprecipitating clouds. The precipitation causes cold pools that disconnect the continuity of the air between the surface and the cloud base. Precipitation also invalidates the radar measurements of updraft.
5. Cases where some of the data were unavailable had to be excluded.

5. Conclusions

The summary of the results, as given in Figure 7, shows good agreement between the satellites with radar-retrieved and ground-based-measured CCN. The number of cases is too small for a meaningful regression analysis. All that can be done here is measuring the root-mean-square error of the fractional deviations, (satellite validation)/validation, of the satellite from the ground-based CCN calculations. The evaluation is done in fractional errors, because the CCN effects on clouds are logarithmic. The fractional estimation errors are 0.13 (i.e., 13%) with respect to the TDMA, 0.26 with respect to the AOS, and 0.27 with respect to the combined AOS and TDMA. The better result for the TDMA is encouraging, because the TDMA measures CCN(S) much more accurately than the AOS CCN chamber, especially at supersaturations $<$0.4%. These are encouraging results. However, due to the small number of available cases, the relation may change somewhat when more cases will be added. However, these results can support the following conclusions:

1. Closure was achieved between surface-measured CCN and remotely sensed cloud base drop concentrations during conditions of well-mixed boundary layer.
2. The closure provides some confidence in the validity of the methodology for retrieving the number of activated CCN based on the vertical evolution of r_e, as measured by the VIIRS imager at a nadir resolution of 375 m.
3. The closure also supports the methodology of weighing the second moment of the cloud base updraft (equation (5)) as the effective updraft for its impact on cloud microstructure.
4. Satellite retrieving of N_a of convective clouds is a new capability. If proven to be viable operationally, this parameter can be ingested into weather prediction models as well as used for developing and validating cloud-aerosol parameterizations.
5. This serves as a proof of concept for a major component of the vision of simultaneous measurements of cloud microstructure and CCN from space by using clouds as natural CCN chambers, which are in the basis of the proposed CHASER satellite [*Rosenfeld et al.*, 2012; *Rennó et al.*, 2013].
6. In order to complete the proof of concept of CHASER, a methodology for satellite estimates of cloud base updraft is yet to be developed and demonstrated.

Acknowledgments

This study was supported by the U.S. Department of Energy Office of Science (BER) Atmospheric System Research program, grant DE-SC0006787. This study is also partially supported by project BACCHUS FP7-603445. Additional support was obtained from the Israeli Space Agency, Ministry of Science and Technology. The authors thank two anonymous reviewers for their helpful comments.

The Editor thanks two anonymous reviewers for their assistance in evaluating this paper.

References

Bennartz, R. (2007), Global assessment of marine boundary layer cloud droplet number concentration from satellite, *J. Geophys. Res.*, *112*, D02201, doi:10.1029/2006JD007547.

Burnet, F., and J. L. Brenguier (2007), Observational study of the entrainment-mixing process in warm convective clouds, *J. Atmos. Sci.*, *64*, 1995–2011.

Freud, E., and D. Rosenfeld (2012), Linear relation between convective cloud drop number concentration and depth for rain initiation, *J. Geophys. Res.*, *117*, D02207, doi:10.1029/2011JD016457.

Freud, E., D. Rosenfeld, and J. R. Kulkarni (2011), Resolving both entrainment-mixing and number of activated CCN in deep convective clouds, *Atmos. Chem. Phys.*, *11*, 12,887–12,900, doi:10.5194/acp-11-12887-2011.

Paluch, I. (1986), Mixing and the cloud droplet size spectrum: Generalizations from the CCOPE data, *J. Atmos. Sci.*, *43*, 1984–1993.

Paluch, I., and D. Baumgardner (1989), Entrainment and fine-scale mixing in a continental convective cloud, *J. Atmos. Sci.*, *46*, 261–278.

Pawlowska, H., J. L. Brenguier, and F. Burnet (2000), Microphysical properties of stratocumulus clouds, *Atmos. Res.*, *55*, 15–33.

Pinsky, M., A. Khain, I. Mazin, and A. Korolev (2012), Analytical estimation of droplet concentration at cloud base, *J. Geophys. Res.*, *117*, D18211, doi:10.1029/2012JD017753.

©2014. American Geophysical Union. All Rights Reserved.

Rennó, N. O., et al. (2013), CHASER: An innovative satellite mission concept to measure the effects of aerosols on clouds and climate, *Bull. Am. Meteorol. Soc.*, *94*, 685–694.

Rosenfeld, D., E. Williams, M. O. Andreae, E. Freud, U. Pöschl, and N. O. Rennó (2012), The scientific basis for a satellite mission to retrieve CCN concentrations and their impacts on convective clouds, *Atmos. Meas. Tech.*, *5*, 2039–2055, doi:10.5194/amt-5-2039-2012.

Rosenfeld, D., G. Liu, X. Yu, Y. Zhu, J. Dai, X. Xu, and Z. Yue (2013), High resolution (375 m) cloud microstructure as seen from the NPP/VIIRS Satellite imager, *Atmos. Chem. Phys. Discuss.*, *13*, 29,845–29,894, doi:10.5194/acpd-13-29845-2013.

Rosenfeld, D., S. Sherwood, R. Wood, and L. Donner (2014), Climate effects of aerosol-cloud interactions, *Science*, *343*, 379–380.

Szczodrak, M., P. H. Austin, and P. B. Krummel (2001), Variability of optical depth and effective radius in marine stratocumulus clouds, *J. Atmos. Sci.*, *58*, 2912–2926.

Zhu, Y., D. Rosenfeld, X. Yu, G. Liu, J. Dai, and X. Xu (2014), Satellite retrieval of convective cloud base temperature based on the NPP/VIIRS Imager, *Geophys. Res. Lett.*, *41*, 1308–1313, doi:10.1002/2013GL058970.

©2014. American Geophysical Union. All Rights Reserved.